A logarithmic bottom boundary layer model for the unsteady and non-uniform swash flow

Fangfang Zhu[a,*], Nicholas Dodd[b], Riccardo Briganti[b], Magnus Larson[c], Jie Zhang[c]

[a] *Department of Civil Engineering, University of Nottingham Ningbo China, 199 Taikang East Road, Ningbo, 315100, China*

[b] *Faculty of Engineering, University of Nottingham, Nottingham NG7 2RD, UK*

[c] *Water Resources Engineering, Lund University, Box 118, 22100, Lund, Sweden*

Abstract

This paper presents a bottom boundary layer model for the unsteady and non-uniform flow in the swash zone, by extending the momentum integral method so as to include spatial gradients. The developed model is further incorporated into a hydrodynamic model based on the Nonlinear Shallow Water Equations. Two swash zone cases are examined to investigate the effect of the inclusion of spatial gradients. In the first of the two, boundary layer development under non-breaking periodic waves formulated by Carrier and Greenspan (1958) is investigated (wave-driven swash). Results show that the spatial gradients have the most pronounced effect in the lower swash, and in the region just seaward. In both these regions the spatial gradients enhance (diminish) onshore (offshore) bed shear stress, thus potentially contributing to onshore sediment transport under non-breaking waves. The second case investigated is the Kikkert et al. (2012) dam-break swash event (bore-driven swash). The model results are qualitatively and quantitatively accurate when compared against the laboratory measurements, and the velocities in the later backwash agree more closely with the measurements than those of Briganti et al. (2011). Results show that the inclusion of spatial gradients also favours onshore sediment transport in the lower swash. In addition, the bottom boundary layer is more fully developed in the uprush tip, resulting in smaller bed shear stress in the upper swash. The extended momentum integral method thus appears to capture more comprehensively the swash boundary layer, and the approach, therefore, offers a way forward in more

accurate reproduction of swash dynamics in computational modelling.

Keywords: swash, spatial gradients, bottom boundary layer, bed shear stress

---

1. Introduction

The swash zone is a very dynamic region of the beach, defined as that part of the beach that is alternately subaerial and subaqueous, where waves run up (shorewards: uprush) and back down (seawards: backwash) the beachface. Consequently the flow is highly unsteady, and there is also considerable sediment transport both as bed and suspended load. The beachface response in this region plays an important role in the sediment exchange between land and sea, markedly affecting the nearshore morphological evolution.

Despite this complexity, the Nonlinear Shallow Water Equations (NSWEs) have proved successful at reproducing many swash and related flows (e.g. Kobayashi and Wurjanto, 1989; Dodd, 1998; Bellotti and Brocchini, 2005). In these studies, the effect of the boundary layer is typically represented by a constant Chezy friction factor, which is usually pre-determined, and related to bed material.

However, the boundary layer, and, in turn, the bed shear stress, are affected by accelerations and pressure gradients within the swash flow (Puleo et al., 2003). Some studies have accounted for these and other effects of complexity in swash flows by resolving the water column (Puleo et al., 2007; Torres-Freyermuth et al., 2013; Briganti et al., 2016; Baldock and Torres-Freyermuth, 2020), but models with this capability are computationally expensive to solve for engineering purposes.

An alternative approach is to improve the description of the bottom boundary layer (BBL), within which most depth variation occurs, whilst retaining the simplicity of the description of the free flow region. Barnes and Baldock (2010) developed a Lagrangian model for the boundary layer development within the swash zone, which is based on the momentum integral approach for steady, flat plate boundary layers and, in addition, it accounts for the unsteadiness of flow and flow history. Briganti et al. (2011) coupled a boundary layer model based on the momentum integral method (Fredsøe and Deigaard, 1993) to the NSWEs, in which the vertical distribution of horizontal velocity was assumed to follow the logarithmic profile. However, the effects due to spatial gradients in velocity and boundary layer thickness were not considered in either study.

The assumption of logarithmic profile of the horizontal velocities in the boundary layer is well supported by experimental studies. O'Donoghue et al. (2010) estimated the bed shear stress in the uprush based on logarithmic profile fitting to the measured velocities from particle image velocimetry (PIV) system, and the results show the estimates agree reasonably well with the corresponding direct shear plate measurements reported by Barnes et al. (2009). Ruju et al. (2016) analysed the near bed horizontal velocities measured by high-resolution Acoustic Doppler Velocity Profilers in laboratory swash flow, and the results show that the horizontal velocities in the boundary layer follow the log law in most swash cycles.

In this work, the BBL model developed by Briganti et al. (2011), which starts from the Fredsøe and Deigaard (1993) model, is extended to include velocity and boundary layer thickness gradients, which in principle would describe more completely the behaviour of the boundary layer in non-uniform flow on impermeable beaches without discontinuous bottom geometry. The effects of spatial gradients on the boundary layer development are here investigated under two different swash events. The first one is the swash event driven by the well known non-breaking periodic waves formulated by Carrier and Greenspan (1958), which allows us to compare the numerical results against the exact solution, and also illustrate the periodic boundary layer development. The second case investigated is the Kikkert et al. (2012) dam-break generated swash event on a fixed impermeable bed, which provides detailed measurements of bed shear stress and near bed velocities.

This paper is organised as follows: after this Introduction, in § 2, we present the model development. We then simulate the non-breaking periodic waves formulated by Carrier and Greenspan (1958) in § 3. The dam-break event examined by Kikkert et al. (2012) in laboratory is investigated in § 4. In § 5, we draw our conclusions.

2. Model development

2.1. Hydrodynamic model

The Nonlinear Shallow Water Equations including bed shear stress are utilised to describe the flow. Therefore, the governing equations are:

$$\frac{\partial h}{\partial t} + u\frac{\partial h}{\partial x} + h\frac{\partial u}{\partial x} = 0, \tag{1}$$

$$\frac{\partial u}{\partial t} + u\frac{\partial u}{\partial x} + g\frac{\partial h}{\partial x} + g\frac{\partial B}{\partial x} = -\frac{\tau_b}{\rho h}, \tag{2}$$

where x (m) represents cross-shore distance, t (s) is time, h (m) represents water depth, u (ms^{-1}) is a depth-averaged horizontal velocity, ρ (kgm^{-3}) is water density, τ_b (kgm^{-1}s^{-2} or Nm^{-2}) is shear stress at the bed, $B = B(x)$ (m) is the bed level (here considered as a function of x), and g (ms^{-2}) is gravity acceleration.

In Fig. 1, we illustrate the general swash geometry that is considered and the main variables utilised. $\eta = h+B$ (m) represents the free surface position from the reference level $z' = 0$.

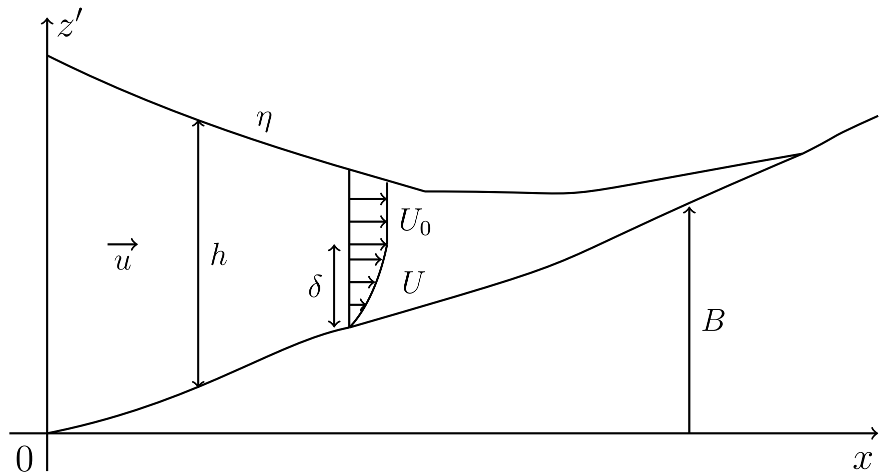

Figure 1: Schematic diagram for a general swash.

2.2. Bottom boundary layer model

The bottom boundary layer is modelled and solved using the momentum integral approach to calculate τ_b in Eq. (2) (Fredsøe and Deigaard, 1993; Briganti et al., 2011).

Inside the boundary layer the horizontal velocity increases from 0 at the bed (due to the no slip condition) to the free stream velocity U_0 at the upper limit of the boundary layer. Therefore, shear stress exists inside the boundary layer because of the relative motion of flow in the vertical direction. However, outside the boundary layer, the flow all moves at the free stream velocity U_0 with no relative motion in the vertical direction, and therefore no shear stress.

Hence, the momentum equation for the flow outside the boundary layer is

$$\frac{\partial U_0}{\partial t} + U_0 \frac{\partial U_0}{\partial x} = -g\frac{\partial h}{\partial x} - g\frac{\partial B}{\partial x}. \tag{3}$$

While the momentum equation for the flow inside the boundary layer is:

$$\frac{\partial U}{\partial t} + U\frac{\partial U}{\partial x} = -g\frac{\partial h}{\partial x} - g\frac{\partial B}{\partial x} + \frac{1}{\rho}\frac{\partial \tau}{\partial z} \tag{4}$$

where z (m) is the vertical distance from the bed ($z = z' - B$), $\tau = \tau(x, z, t)$ is shear stress at location (x,z) at time t. U (ms^{-1}) is the horizontal velocity inside the boundary layer, which is approximated using the logarithmic law

$$U(x, z, t) = \frac{U_f}{\kappa} \ln\left(\frac{z}{z_0}\right), \tag{5}$$

where $\kappa = 0.4$ is the von Karman's constant, and U_f (ms^{-1}) is the friction velocity,

$$U_f = U_f(x, t) = \frac{U_0}{|U_0|}\sqrt{\mid \tau_b \mid / \rho}. \tag{6}$$

z_0 (m) is the vertical distance from the bed at which the velocity is assumed to be 0, and here $z_0 = K_n/30$ with K_n (m) being the bed roughness.

At the upper limit of the boundary layer, i.e., $z = z_0 + \delta$ with δ the boundary layer thickness, the velocity equals the free stream velocity. Thus,

$$U(x, z = z_0 + \delta, t) = U_0 = \frac{U_f}{\kappa} \ln\left(\frac{z_0 + \delta}{z_0}\right) = \frac{U_f}{\kappa} Z \tag{7}$$

where $Z = \ln\left(\frac{\delta+z_0}{z_0}\right)$. Note that $U_0 = U_0(h, u, Z(\delta))$, and the derivation is shown in Appendix A, which itself stems from assuming Eq. (5). Note that the expression of the free stream velocity U_0 (Eq. (A.8)) for the case of $\delta > h$ is slightly different from that in Briganti et al. (2011) because of different integration bounds used to obtain depth-averaged velocity u.

In the case of uniform flow, $\frac{\partial U_0}{\partial x} = 0$ and $\frac{\partial U}{\partial x} = 0$, and Eqs. (3) and (4) reduce to the equations used by Fredsøe and Deigaard (1993) and Briganti et al. (2011), who examined the boundary layer development under non-uniform flows but assuming that $\frac{\partial U_0}{\partial x} = 0$ and $\frac{\partial U}{\partial x} = 0$. See Fredsøe and Deigaard (1993) and Briganti et al. (2011) for further details on the calculation of τ_b from the simplified equations.

In this work the spatial gradients in U_0 and U are taken into consideration for flows of non-uniform velocities, so subtracting Eq. (3) from Eq. (4) gives

$$\frac{\partial}{\partial t}(U_0 - U) + \frac{\partial}{\partial x}\left(\frac{1}{2}U_0^2 - \frac{1}{2}U^2\right) = -\frac{1}{\rho}\frac{\partial \tau}{\partial z}. \tag{8}$$

Integrating Eq. (8) across the boundary layer $[z_0,\, z_0 + \delta]$ gives

$$\frac{\tau_b}{\rho} = \int_{z_0}^{z_0+\delta} \frac{\partial}{\partial t}(U_0 - U)dz + \int_{z_0}^{z_0+\delta} \frac{\partial}{\partial x}\left(\frac{1}{2}U_0^2 - \frac{1}{2}U^2\right) dz. \tag{9}$$

The second term on the right hand side is the extra term compared to the uniform flow case, and it accounts for the effect of the spatial gradient on the bed shear stress.

Using Eq. (7) and the definition of U_f by Eq. (6) we then arrive at a differential equation for Z from Eq. (9),

$$\frac{\partial Z}{\partial t} + \frac{U_0}{f_2 Z}\left(f_1 + f_2(Z-1)\right)\frac{\partial Z}{\partial x} = \frac{\kappa^2}{z_0 f_2}|U_0| - \frac{f_1 Z}{f_2 U_0}\frac{\partial U_0}{\partial t} - \frac{\left(f_2 + f_1(Z-1)\right)}{f_2}\frac{\partial U_0}{\partial x}, \tag{10}$$

where $f_1 = e^Z - Z - 1$ and $f_2 = Ze^Z - e^Z + 1$. Note that $f_1,\ f_2,\ f_2 + f_1(Z-1),\ f_1 + f_2(Z-1) \geq 0$. The equal signs hold true only when $Z = 0$, i.e., when BBL thickness $\delta = 0$.

Eq. (10) can be rewritten as:

$$\begin{aligned} \frac{dZ}{dt} \quad &= \quad \frac{\kappa^2}{z_0 f_2}|U_0| - \frac{f_1 Z}{f_2 U_0}\frac{dU_0}{dt}, \\ \text{where} \quad & \frac{dx}{dt} = \frac{U_0}{f_1 Z}\left(f_2 + f_1(Z-1)\right) \ \text{for}\ \frac{dU_0}{dt} \\ & \frac{dx}{dt} = \frac{U_0}{f_2 Z}\left(f_1 + f_2(Z-1)\right) \ \text{for}\ \frac{dZ}{dt}. \end{aligned} \tag{11}$$

If the spatial gradients of U_0 and Z are neglected, the characteristic speeds $\frac{dx}{dt} = 0$ for both $\frac{dU_0}{dt}$ and $\frac{dZ}{dt}$, therefore we recover partial time derivatives in Eq. (11), which describe variation in time at one location, as used by Briganti et al. (2011). Eq. (11) is solved for Z, which then gives τ_b via Eqs. (6) and (7). The calculation of bed shear stress at the tip (wet-dry boundary) is detailed in Appendix B. Note that the bed shear stress $\tau_b \to \infty$ for the boundary layer thickness $\delta \to 0$, which gives an unbounded friction coefficient $c_d = \frac{|\tau_b|}{\rho u^2}$. Therefore, we limit the bed shear stress in these circumstances: the maximum friction coefficient of $c_d = 0.0597$ is imposed. The value of $c_d = 0.0597$ comes from Appendix B.

In Eq. (11) it can be seen that Z is advected at a speed related to, but different from, U_0, which can be thought of as being due to the slower flow within the boundary layer. Note that $dx/dt \to 2U_0/3$ as $Z \to 0$, so advection occurs immediately, and that dx/dt increases for increasing boundary layer thickness such that $dx/dt \to U_0$ as $Z \to \infty$. Thus a boundary layer can grow (decay) at one location if a more (less) developed boundary layer is advected by the flow into this location. This extra term is the second on the LHS of Eq. (10).

Inclusion of the spatial terms also allows the boundary layer to evolve due to spatial gradients in U_0. This can be interpreted as advective acceleration of the free flow, which is now present in addition to the local acceleration. This extra term is the last on the RHS of Eq. (10); note, however, that this speed also depends on the boundary layer thickness through Z. Onshore (offshore) flow acceleration of the uprush (backwash) thins the boundary layer, with the corresponding deceleration thickening it.

Finally, the boundary layer can also grow locally due to steady current; the first term on the RHS of Eq. (10) is always > 0 in both uprush and backwash, and so it always promotes growth.

2.3. Analysis of boundary layer development

2.3.1. Flow inundation ($U_0 \neq 0$ and $Z = 0$)

When a dry bed is first inundated, we have $Z = 0$ and $U_0 \neq 0$. Eq. (10) shows that when $Z \to 0$, $\frac{\partial Z}{\partial t} \to -\frac{2}{3}U_0\frac{\partial Z}{\partial x} + \frac{\kappa^2}{z_0 f_2}|U_0| \to +\infty$. This implies that Z immediately attains a finite value at inundation (at which the growth rate becomes finite). Therefore, at the initial time, Z is set to a small value to avoid singularity problems. Tests of different initial Z values show convergence, and are not included here. The asymptotic approximation for Z at inundation (see Appendix C) can provide an initial approximation.

2.3.2. Flow reversal ($U_0 = 0$)

At flow reversal, $U = 0$ and $U_0 = 0$ are assumed in the present BBL model. When $U_0 \to 0$, Eq. (10) can be simplified into

$$\frac{\partial Z}{\partial t} \sim -\frac{Zf_1}{U_0 f_2}\frac{\partial U_0}{\partial t} - \frac{f_2 + f_1(Z-1)}{f_2}\frac{\partial U_0}{\partial x}. \quad (12)$$

When flow changes from onshore to offshore, $\frac{\partial U_0}{\partial t} < 0$. Just before reversal, $U \to 0^+$, and $\frac{\partial Z}{\partial t} \to +\infty$. This implies that before flow reversal from onshore to offshore directed, Z increases rapidly, thus the boundary layer thickness grows to occupy the whole water column and becomes depth limited. After flow reversal, i.e., $U \to 0^-$, $\frac{\partial Z}{\partial t} \to -\infty$, Z, thus the boundary layer thickness, δ, rapidly decreases to 0. Therefore, when flow changes from onshore to offshore directed, we set $\delta = 0$.

Similarly, when flow direction changes from offshore to onshore, the boundary layer grows to the full water column before reversal, and δ is set to 0 after reversal.

2.4. Shock conditions

Shocks frequently develop in the swash flow, i.e., the flow variables have jump discontinuity. The partial differential governing equations (1) and (2) cannot be applied at discontinuous flow, and so shock conditions are required. Applying the mass and momentum conservation across a shock, i.e., a bore, gives the Rankine-Hugoniot conditions:

$$-W(h_R - h_L) + (h_R u_R - h_L u_L) = 0, \quad (13)$$

$$-W(h_R u_R - h_L u_L) + \left(h_R u_R^2 + \frac{1}{2}g h_R^2 - h_L u_L^2 - \frac{1}{2}g h_L^2\right) + \frac{1}{2}g(h_R + h_L)(B_R - B_L) = 0, \quad (14)$$

where the subscripts L and R represent the left and right sides of the bore, W is the shock velocity, and to get Eq. (14), the Needham and Hey (1991) approximation, i.e., $\int_{B_L}^{B_R} h dB = \frac{1}{2}(h_L + h_R)(B_R - B_L)$, is applied. The shock condition for δ is derived in Appendix D.

2.5. Numerical scheme

The flow chart in Fig. 2 illustrates the numerical scheme for solving depth-averaged flow and flow in the bottom boundary layer. Eqs. (1) and (2), with

h, u, and τ_b from the previous time step are solved by the Specified Time Interval Method of characteristics (STI MOC) to get h and u at the new time step (Zhu and Dodd, 2015). At shocks, the conditions Eqs. (13) and (14) together with the Riemann equations derived from Eqs. (1) and (2) are solved to obtain h_L, u_L, h_R, u_R and W. Note that the shock condition Eq. (D.4) for δ is not solved simultaneously because the boundary layer is solved after the depth-averaged flow as shown in Fig. 2.

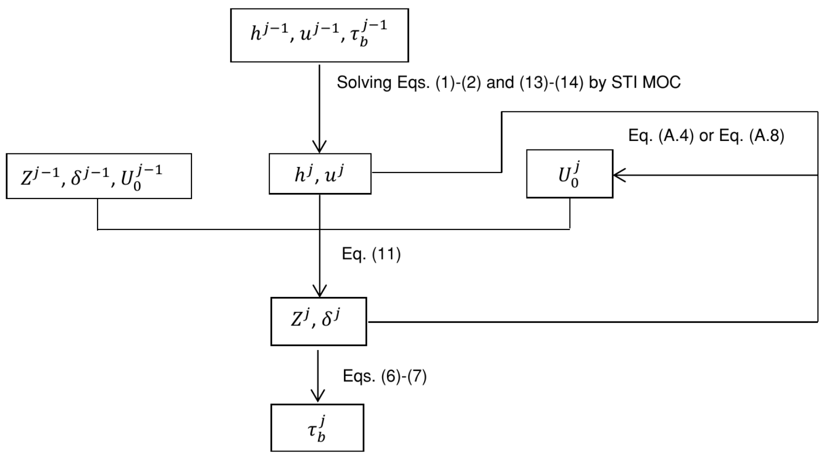

Figure 2: Flow chart of the numerical algorithm during a single time step. The superscripts $j-1$ and j indicate the time step.

Water depth h and depth-averaged velocity u at the new time step, and δ from the previous time step, are used to calculate the first approximate value of free stream velocity U_0 at the new time step (Appendix A), which is then updated with the newly calculated δ at the new time step. With Z and U_0 at the old time step and U_0 at the new time step, Eq. (11) is solved to update Z using the characteristic method, and τ_b is calculated for the new time step, thus completing the cycle. At shocks, the boundary layer thickness δ at the downstream side cannot be calculated because the characteristic lines cross over the shock. Thus, the shock condition Eq. (D.4) is used to calculate δ on the downstream side.

It should be noted that for uniform flows, or if spatial gradients in u and Z are ignored, the equations in the present work reduce to those in Briganti et al. (2011). However, the numerical methods for the hydrodynamic model and boundary layer model in this work are different from those in Briganti et al. (2011). Therefore, the numerical results without spatial gradients obtained in this work are not necessarily identical to those in Briganti et al. (2011).

3. Carrier and Greenspan (1958) periodic waves simulation

The non-breaking periodic waves formulated by Carrier and Greenspan (1958) are simulated to investigate the development of a boundary layer under periodic waves in the swash.

In the numerical simulation, the computational grid size is $\Delta x = 0.01$ m, and the time interval is $\Delta t = 6.39 \times 10^{-4}$ s for numerical implementation. In the boundary layer simulation, $z_0 = 1 \times 10^{-4}$ m is employed for the vertical distance at which the velocity is assumed to be 0.

3.1. Formulation and exact solution

We follow Mungkasi and Roberts (2012) to obtain the exact solution. The nondimensionalization in Mungkasi and Roberts (2012) is used and the dimensionless variables are indicated by the subscript $*$.

The velocity potential of the periodic waves is

$$\phi(\chi_*, \lambda_*) = A_* J_0(\omega_* \chi_*) \cos(\omega_* \lambda_*), \tag{15}$$

where A_* is dimensionless wave amplitude, χ_* and λ_* are two dimensionless hodograph variables, a space-like and a time-like coordinate, respectively, J_0 is the zeroth order Bessel function of the first kind. ω_* is wave frequency,

$$\omega_* = \frac{\pi}{T_*}, \tag{16}$$

where T_* is the wave period.

Here we take $A_* = 0.8$, beach slope $\tan\alpha = 0.1$, dimensional wave period $T = 10$ s, and $x = 0$ m as the seaward boundary for the periodic wave. The dimensionless exact solutions are then converted to the dimensional values.

The exact solutions (Mungkasi and Roberts, 2012; Carrier and Greenspan, 1958) are used as the initial and seaward boundary conditions for the simulation. A verification at the shoreline against the Mungkasi and Roberts (2012) solution is shown in Appendix E. In the simulations the region 8 m $\lessapprox x \lessapprox$ 12 m comprises the swash zone. $0 \leq t \leq \frac{1}{2}T$ belongs to backwash, and $\frac{1}{2}T \leq t \leq T$ belongs to uprush.

Finally, here the hydrodynamics are assumed not to be affected by bed shear stress so that the Mungkasi and Roberts (2012) solution is maintained; the boundary layer development is the focus here.

3.2. Boundary layer development

3.2.1. Spatial variation

Snapshots of η, u, δ, $|\tau_b|$, and $\tau_{b,wo}/\tau_{b,w}$ (ratio of bed shear stress without ($\tau_{b,wo}$) and with ($\tau_{b,w}$) spatial gradients) over one period are shown in Fig. 3. The symmetry in the Carrier-Greenspan solution in uprush and backwash can be seen in Fig. 3(a) and (b): $\eta(x, \frac{T}{2} - \epsilon) = \eta(x, \frac{T}{2} + \epsilon)$, and $u(x, \frac{T}{2} - \epsilon) = -u(x, \frac{T}{2} + \epsilon)$ for $0 \leq \epsilon \leq \frac{T}{2}$. Fig. 3(b) shows that the velocity gradient is positive in the uprush, and negative in the backwash.

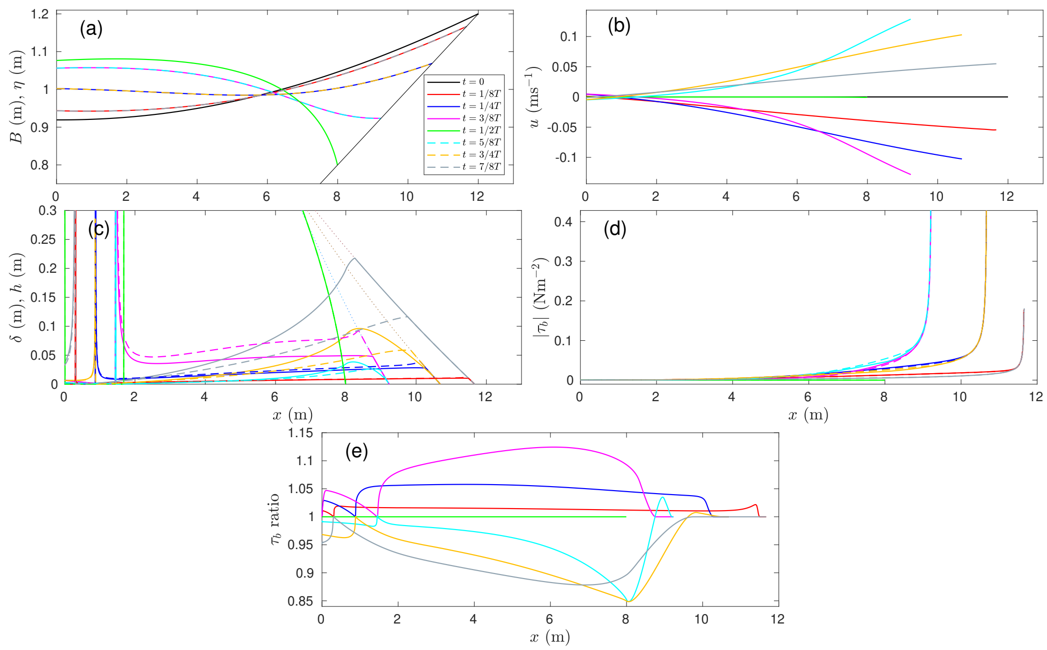

Figure 3: The snapshots of (a): B and η, (b): u, (c): δ and h, (d): $|\tau_b|$, and (e): $\tau_{b,wo}/\tau_{b,w}$, during periodic waves propagating towards the shore. In (c), solid line: boundary layer thickness without spatial gradients; dashed line: boundary layer thickness with spatial gradients; dotted line: water depth. In (d): solid line: without spatial gradients; dashed line: with spatial gradients.

Because the vertical velocity structure in Eq. (7) is always assumed for flow in the boundary layer, this implies that any difference between τ_b (Fig. 3(d)) in uprush and backwash must be due to differences in δ (Fig. 3(c)). If we focus first on δ without spatial gradients (solid lines in Fig. 3(c)), clear differences between δ in uprush and backwash can be seen, both in the swash

($x \geq 8$ m) and further seaward. There is more spatial variation in δ in uprush than in backwash, and δ is overall thicker in the uprush.

Boundary layer thickness δ in the late uprush ($t = 3/4T$ and $7/8T$) is larger than values at the same locations in the early backwash ($t = 1/4T$ and $1/8T$), where the depth is the same, because of the different flow histories (decelerating from a finite value in the late uprush, and accelerating offshore from zero in the early backwash). For similar reasons the boundary layer is more developed in late backwash ($t = 3/8T$) than in the early uprush ($t = 5/8T$).

Fig. 3(c) shows that the boundary layer thickness increases in the onshore direction, in both uprush and backwash, although much more so in the uprush, until becoming depth limited at the tip. This is because u increases in magnitude toward the shore $\left(\frac{\partial Z}{\partial t} \sim \frac{\kappa^2}{z_0 f_2}|U_0|\right)$, and local flow acceleration effects play a large role too, yielding a much more spatially uniform boundary layer in the backwash.

The inclusion of the spatial gradients yields a significantly more spatially uniform δ in the uprush, with a smaller opposite effect in the backwash. These effects are consistent with the mostly positive (negative) gradient in u and therefore U_0 in the uprush (backwash) through the final term in Eq. (10). The large spatial gradients in δ in the uprush obtained without spatial gradients (solid lines of Fig. 3(c)) also act to advect the thinner boundary layer shoreward when spatial gradients are included.

Fig. 3(d) shows the corresponding $|\tau_b|$ values. The bed shear stress increases in magnitude rapidly toward the tip of the swash, where the velocities are large and water depths are small. Fig. 3(e) illustrates the ratio of the bed shear stress in the simulation without spatial gradients to that with spatial gradients. In the backwash, the bed shear stresses without spatial gradients are larger than those with spatial gradients, while the opposite trend is observed in the uprush. The differences are particularly exaggerated at the base of the swash, where the spatial gradients in the early to mid uprush provide an additional onshore-directed bed shear stress.

3.3. Temporal variation

The time series of h, u, δ and τ_b at the seaward extent of the swash $x = 8$ m is shown in Fig. 4. We can see that the boundary layer varies periodically, and is different in the uprush and backwash. At the start of the backwash we see δ grow after flow reversal. This growth is eventually curtailed by the

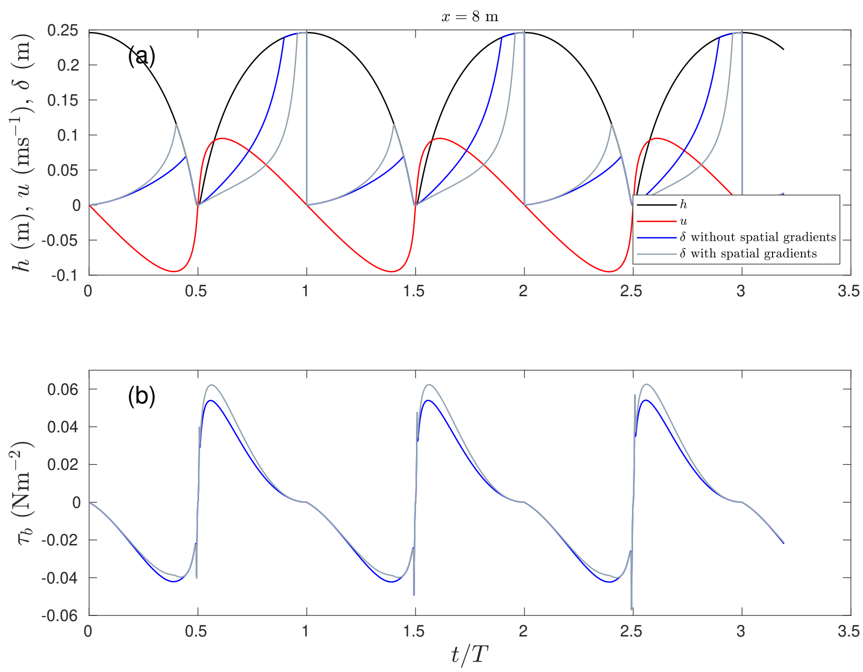

Figure 4: The time series of h, u, δ and τ_b at the seaward extent of swash $x = 8$ m during periodic waves propagating towards the shore.

water depth. At the subsequent flow reversal the boundary layer develops again from zero, and so grows again in the uprush, more quickly, because of the rapid increase in u. There is an abrupt change in the boundary layer thickness at flow reversal. However, the 0 velocity at flow reversal results in continuous bed shear stress.

The boundary layer is noticeably thicker in the uprush than in the backwash. This is because in the uprush the flow accelerates more rapidly after reversal than in the backwash (see Fig. 4(b)) to a larger velocity, which results in faster boundary layer development.

In Fig. 4(a) we can also see the difference between δ predicted by equations with and without spatial gradients. In the backwash the inclusion of the spatial gradients causes the boundary layer to grow faster than it would otherwise, because of the negative spatial velocity gradient, and also because of the positive spatial gradient in δ and seaward advection of boundary layer. The difference in δ becomes most noticeable in the late backwash. In contrast, in the uprush the inclusion of spatial gradients retards the growth in δ, because now the thinner boundary further seaward is advected into the swash and also because the positive velocity gradient retards the development of the boundary layer.

Fig. 4(b) shows the corresponding τ_b. The peak in τ_b in the backwash occurs toward its end, because U_0 increases slowly from zero. Thus the local acceleration controls the very early development of δ (see Appendix C) and τ_b only develops gradually as U_0 increases. In contrast, the rapidly increasing velocity at the start of the uprush at x =8 m yields a more rapid development in δ, but τ_b develops quicker still, because of the simultaneous very thin boundary layer ($\tau_b \propto U_0^2 Z^{-2}$, Eq. (7)). Note also the asymmetry in the peaks in τ_b (compared to the symmetry in u–red lines in Fig. 4(a)) in uprush and backwash without the inclusion of spatial gradient effects (blue lines in Fig. 4(b)). Again, this is due to the different flow histories in uprush and backwash, and was also found from measurements (Barnes et al., 2009). Therefore, we observe an enhanced onshore bed shear stress at the base of the swash, and therefore expect potentially slightly more onshore sediment transport especially of larger sediment diameters.

This asymmetry between τ_b in uprush and backwash is enhanced with the inclusion of spatial gradients, consistent with Fig. 3(e). In the uprush, as noted earlier, gradients in both U_0 and Z favour a thinner boundary layer, therefore further enhancing the increased τ_b in that phase of the swash. In contrast, in the backwash the difference in δ only becomes noticeable gradually because the flow starts from rest, and only in the late backwash does this lead to a diminution in offshore directed τ_b.

The time series further offshore (Fig. 5) display similar features, but with the differences between results with and without spatial gradients (as well as differences between uprush and backwash) being less pronounced. This is because the free flow is more sinusoidal. Nonetheless, there is a similar shift favouring increased onshore over offshore bed shear stresses.

Finally, further onshore (Fig. 6) we see that in the uprush there is an instantaneous increase to maximum velocity as x = 10 m is wetted. The identical velocity maximum occurs at the end of the backwash. Spatial boundary layer gradient effects are very minor. τ_b increases instantaneously ($\tau_b \sim (t - t_0)^{-2/3}$, where t_0 is time of inundation (see Appendix C and Eq. (7))).

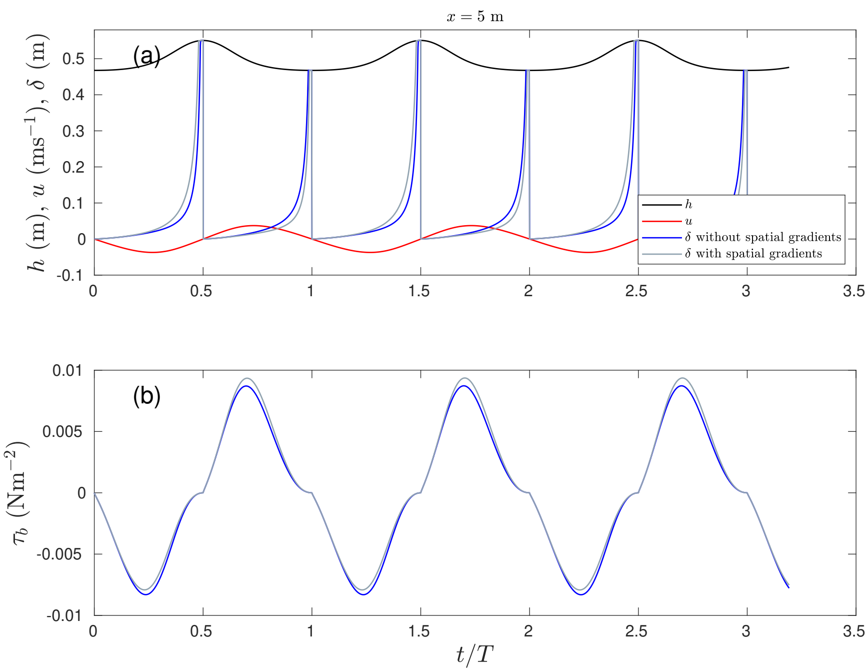

Figure 5: The time series of h, u, δ and τ_b seaward of the swash, $x = 5$ m, during periodic waves propagating towards the shore.

4. Kikkert et al. (2012) swash event

The experiment of a dam-break swash event on a rough, impermeable beach carried out by Kikkert et al. (2009, 2012) in the laboratory, which was considered by Briganti et al. (2011), is utilised in this work to test the BBL model. This allows the comparison of boundary layer structure against experimental measurements and also numerical results from Briganti et al. (2011) for bore-driven swash. The initial set up of the Kikkert et al. (2012) experiment is shown in Fig. 7. The beach is rough and impermeable, and consists of a flat part, and a sloping part of slope 1/10.

We follow Briganti et al. (2011) by driving the simulation with the measured water depths h and depth-averaged velocities u at PIV 1 ($x = -1.802$ m) shown in Fig. 8. The IMP015 case is simulated (Briganti et al., 2011), in which the sediment sizes are $D_{10} = 1.0$ mm, $D_{35} = 1.2$ mm, $D_{50} = 1.3$ mm, $D_{65} = 1.5$ mm, $D_{84} = 1.8$ mm and $D_{90} = 1.9$ mm. The bed roughness $K_n = 2D_{65} = 3$ mm is estimated using the Engelund and Hansen (1967)

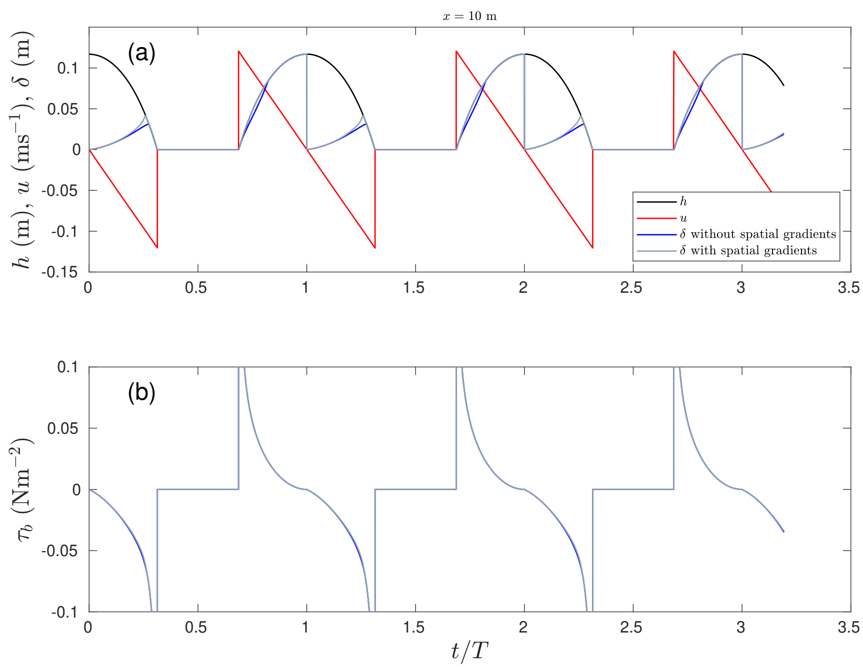

Figure 6: The time series of h, u, δ and τ_b in the upper swash zone $x = 10$ m during periodic waves propagating towards the shore.

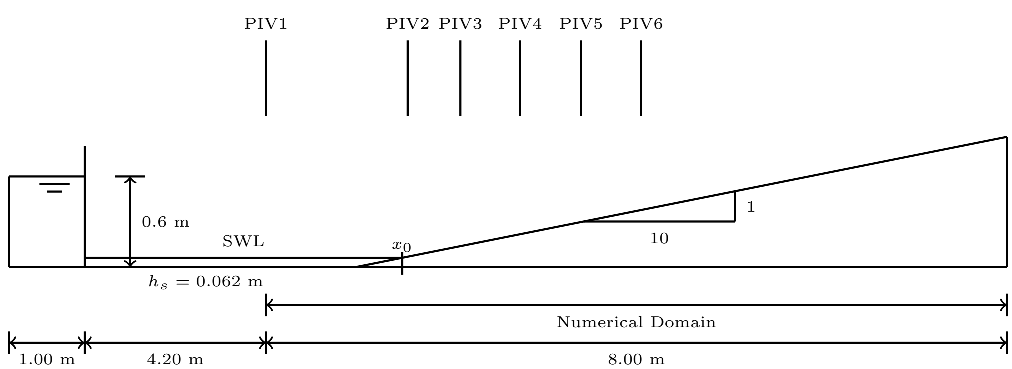

Figure 7: The initial set up of the Kikkert et al. (2012) swash event (Briganti et al., 2011).

formula. Therefore, $z_0 = K_n/30 = 1 \times 10^{-4}$ m.

Finer computational grid size $\Delta x = 0.005$ m and smaller time interval $\Delta t = 3.19 \times 10^{-4}$ s, compared to those used in Carrier and Greenspan (1958) simulation, are used in this simulation because there is shock development

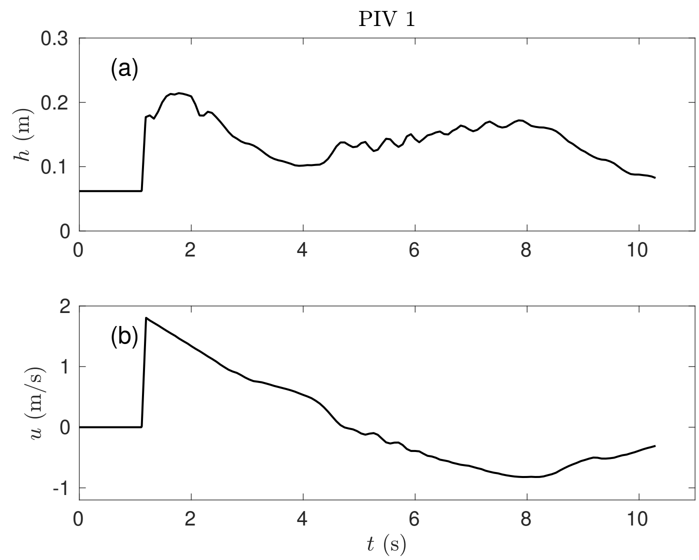

Figure 8: Time series of water depth h and depth-averaged u at PIV 1.

in this dam-break driven swash event.

4.1. Shoreline movement

The comparison for shoreline movement is shown in Fig. 9. The contours of $h = 0.005$ m, corresponding to the value chosen to identify the measured shoreline, for both BBL models (with and without spatial gradients) are in close agreement with the measured shoreline position, and better comparison is achieved compared to Briganti et al. (2011). The modelled shorelines of $h = 0.001$ m and 0 m, retreat much slower in the backwash compared to those of $h = 0.005$ m, indicating very thin backwash flows in the swash zone. The shoreline positions of both $h = 0.001$ m and 0.005 m predicted by Briganti et al. (2011) are retreating faster in the backwash.

The maximum run-ups predicted in the present work are close to the measured value with the relative errors of 0.15% and 1.7% in $h = 0.005$ m for the simulations without and with spatial gradients. When spatial gradients are included, the maximum run-up is slightly larger indicating the relatively smaller bed shear stress.

The Root Mean Squared Error (RMSE) values of the numerical shoreline positions of $h = 0.005$ m against the measured ones are calculated for

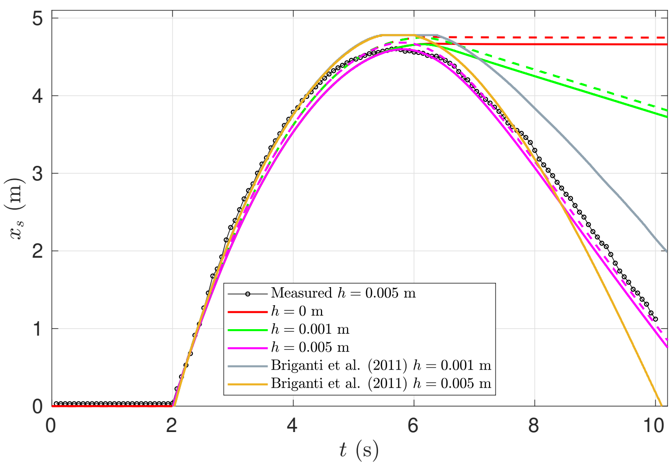

Figure 9: Comparison of the measured (circles) and simulated (solid and dashed lines) shoreline movement of the swash event. Solid line: without spatial gradients; dashed lines: with spatial gradients.

quantitative analysis,

$$\mathrm{RMSE}_{xs} = \sqrt{\frac{\sum_{i=1}^{N_{xs}} (x_{s,mi} - x_{s,ni})^2}{N_{xs}}}, \tag{17}$$

where N_{xs} is the number of measured shoreline positions $x_{s,m}$, and $x_{s,mi}$ ($x_{s,ni}$) is the ith measured (numerically modelled) shoreline position. The RMSE values are shown in Table. 1, which suggest overall good agreement of all numerical results with the measured ones, and closer agreement of the present model results.

Table 1: RMSE values of the shorelines of $h = 0.005$ m calculated from the present model results and those of Briganti et al. (2011).

Simulation	RMSE_{xs}
Without spatial gradients	2.35×10^{-2}
With spatial gradients	1.01×10^{-2}
Briganti et al. (2011)	6.90×10^{-2}

4.2. Spatial variation

The snapshots of the modelled swash lens at different times are shown in Fig. 10. They are in close agreement with Briganti et al. (2011). Also shown on these plots is the top of the boundary layer as predicted by momentum integral method with (grey) and without (red) spatial gradients included. The overall picture is of the boundary layer occupying the whole water column in the mid- to late run-up, and growing more slowly and more uniformly in the backwash, consistent with the Carrier-Greenspan case.

4.3. Time series

The time series of h and u at PIV 2, 4 and 5, the positions of which are $x = 0.072$ m, 1.229 m, 2.356 m respectively, are compared against the measurements and numerical results from Briganti et al. (2011) in Fig. 11. Note that the results with spatial gradients are very close to those without spatial gradients, and therefore not included in Fig. 11. This indicates that the inclusion of spatial gradients in the BBL model have negligible effects on the hydrodynamics in this case. Fig. 11 shows that the present numerical results, and those of Briganti et al. (2011), overpredict the water depths throughout the swash. The simulated results in the present work correspond very closely to those from Briganti et al. (2011) in the uprush, while the velocities in the backwash are closer to the measured values than those from Briganti et al. (2011). The discrepancies in the numerical backwash velocities are probably attributable to different numerical solver and especially different shoreline treatment in Briganti et al. (2011) from the present work. The shoreline motion shown in Fig. 9 illustrates clearly the faster offshore movement of the shoreline in the backwash predicted by Briganti et al. (2011). This perhaps results in the larger offshore velocities at PIV 2, 4 and 5. Furthermore, the expression for U_0 used when $\delta = h$, which occurs in the later stage of the backwash, in the boundary layer model in Briganti et al. (2011), differs slightly from the one in the present work.

The RMSE values of the numerical results h and u against the measured results are calculated for quantitative analysis,

$$\mathrm{RMSE}_h = \sqrt{\frac{\sum_{i=1}^{N_h}(h_{mi} - h_{ni})^2}{N_h}}$$

$$\text{and} \quad \mathrm{RMSE}_u = \sqrt{\frac{\sum_{i=1}^{N_u}(u_{mi} - u_{ni})^2}{N_u}} \tag{18}$$

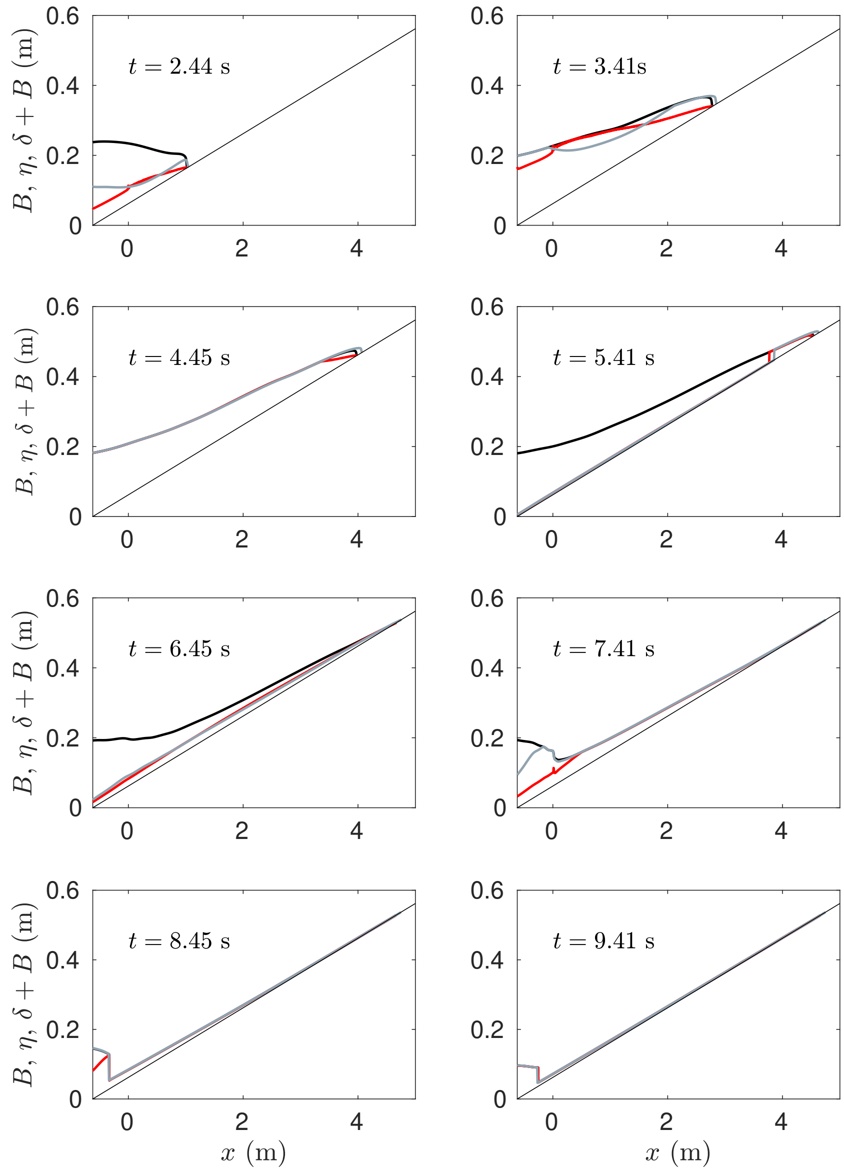

Figure 10: Snapshots of the modelled swash flow (B, η and $B+\delta$) at different times. Thin black lines: B; thick black lines: η without spatial gradients; red lines: $B+\delta$ without spatial gradients; and grey lines: $B+\delta$ with spatial gradients.

444 where N_h (N_u) is the number of points of measured water depths h_m (velocities u_m), h_{mi} (u_{mi}) is the ith measured water depth (velocity), and h_{ni} (u_{ni})

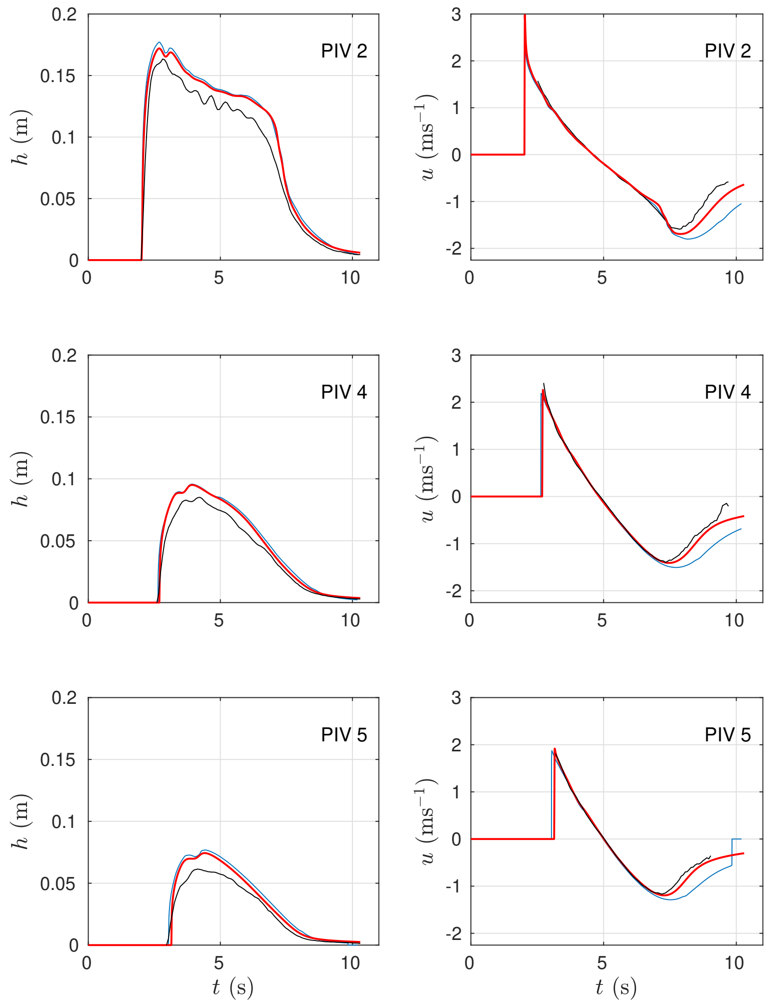

Figure 11: The comparison of time series of water depth h and depth-averaged velocity u at PIV 2, 4 and 5. Black: measured; blue: Briganti et al. (2011); red: present work (only results for the simulation without spatial gradients are shown).

is the ith modelled water depth (velocity). The RMSE values for h and u at PIV 2, 4, 5 calculated from both the present model results and Briganti et al. (2011) results are shown in Table 2. The RMSE values are generally small: for h they are of the order of 0.001 m, and those of u are of the order 0.01 ms^{-1}. The smaller RMSE values for the present model results suggest closer agreement with the measurements than Briganti et al. (2011), which is consistent with the comparison in Fig. 11.

Table 2: The RMSE values of the modelled time series results of h and u at PIV 2, 4, and 5.

	h		
Simulation	PIV2	PIV4	PIV5
Without spatial gradients	1.51×10^{-4}	4.89×10^{-5}	4.51×10^{-5}
With spatial gradients	1.52×10^{-4}	4.49×10^{-5}	3.96×10^{-5}
Briganti et al. (2011)	1.06×10^{-3}	2.38×10^{-4}	1.51×10^{-4}
	u		
Without spatial gradients	2.03×10^{-2}	9.67×10^{-3}	3.52×10^{-3}
With spatial gradients	2.32×10^{-2}	1.14×10^{-2}	5.25×10^{-3}
Briganti et al. (2011)	9.24×10^{-2}	6.96×10^{-2}	4.01×10^{-2}

4.4. Boundary layer development

Fig. 12 shows the contour plots for h, u and δ in the swash event. It can be seen that there are three shocks forming: an incoming bore, a reflecting shock, and a backwash bore, which changes its direction of movement and becomes an incoming bore (Fig. 12(b)).

Both Fig. 12(c) and (d) show the rapid development of the boundary layer in the uprush, the flow reversal, at which the boundary layer growth is assumed to re-start, and its development once more later in the backwash. The difference between Fig. 12(c) and (d) shows the effect of the spatial gradient terms. In the uniform simulation the boundary layer grows only due to local conditions, and does so in the uprush at a fairly uniform rate (note that the contours in δ are approximately equidistant in time for all x), until it becomes depth limited. In contrast, boundary layer thinning and thickening can be observed when spatial gradients are included. The thinner boundary layer in the early uprush is caused by the positive gradients in U_0 (advective accelerations), which, however, are subsequently overcome by the mostly negative spatial gradients in Z, which thicken the boundary layer in the later uprush. Note also that later in the swash, spatial gradients cause the boundary layer to occupy the whole water depth near to the tip, consistent with Fig. 10 at $t = 2.44$ s, and 3.41 s. In the backwash the main difference is caused by the increase in δ seaward of the backwash bore via the shock conditions, as U_0 decreases.

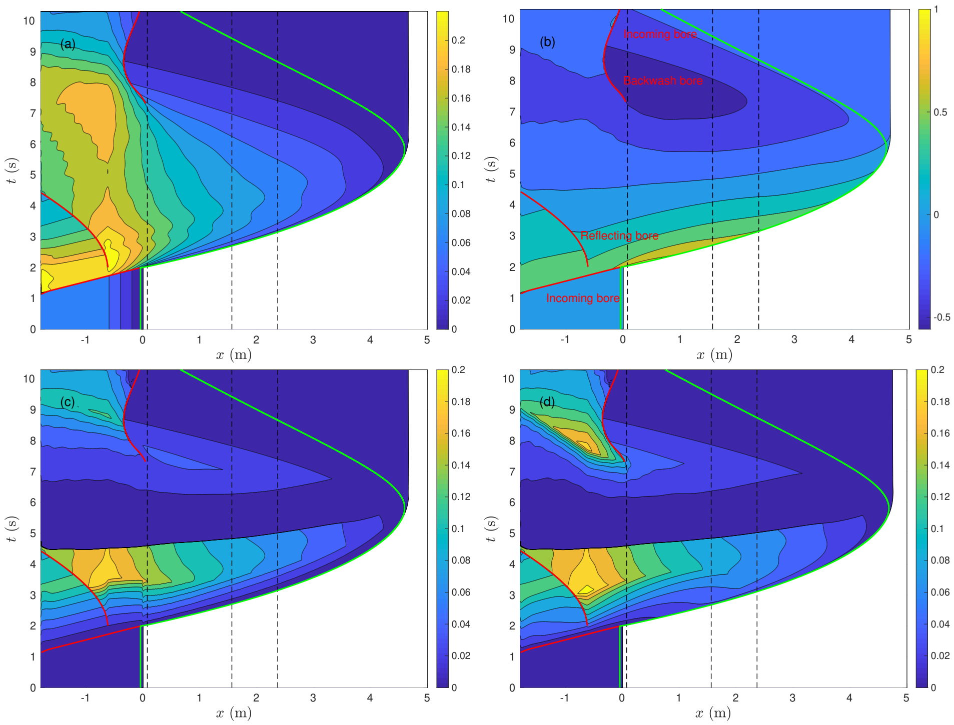

Figure 12: Contour plots for h (a), u (b), and δ (c, d). (c): without spatial gradients, and (d): with spatial gradients. The red lines represent the shock paths, and the green line represents the shoreline position of $h = 0.005$ m.

Fig. 13 shows the evolution of boundary layer at PIV 2, 4, 5 in the simulations with and without spatial gradients. In the uprush, if $\frac{\partial u}{\partial x} = 0$ and $\frac{\partial Z}{\partial x} = 0$ are assumed, the boundary layer thickness at PIV 2 gradually increases, and reaches the whole water column after some time. When spatial gradients in u and Z are considered, the boundary layer at PIV 2 increases at a similar rate in the early stage of inundation, due to the combined effect of boundary layer advection and positive velocity gradient, which counteract each other. It later rapidly increases to the whole water column. This is due to the arrival of the boundary layer feature extending shoreward from the reflected bore (Fig. 12(d)). The backwash at PIV2 is qualitatively similar to that observed for the Carrier-Greenspan case at $x = 5$ and 8 m, with slow growth in δ from 0 followed by spatial gradients creating a thicker δ later on, due to $\frac{\partial u}{\partial x}$.

As we move into the mid- and upper swash (Fig. 13(b) PIV 4 and (c) PIV 5) we see that advection increasingly implies that the boundary layer is fully developed in the uprush. This is consistent with the conclusion drawn by Baldock (2018) and Baldock and Torres-Freyermuth (2020) that the boundary layer near the tip is not locally developed but advected. The backwash at PIV4 and PIV5 also shows growth qualitatively similar to that in PIV2, but δ for the non-uniform case is now slightly smaller than its uniform equivalent, in contrast to PIV2 and the Carrier-Greenspan case.

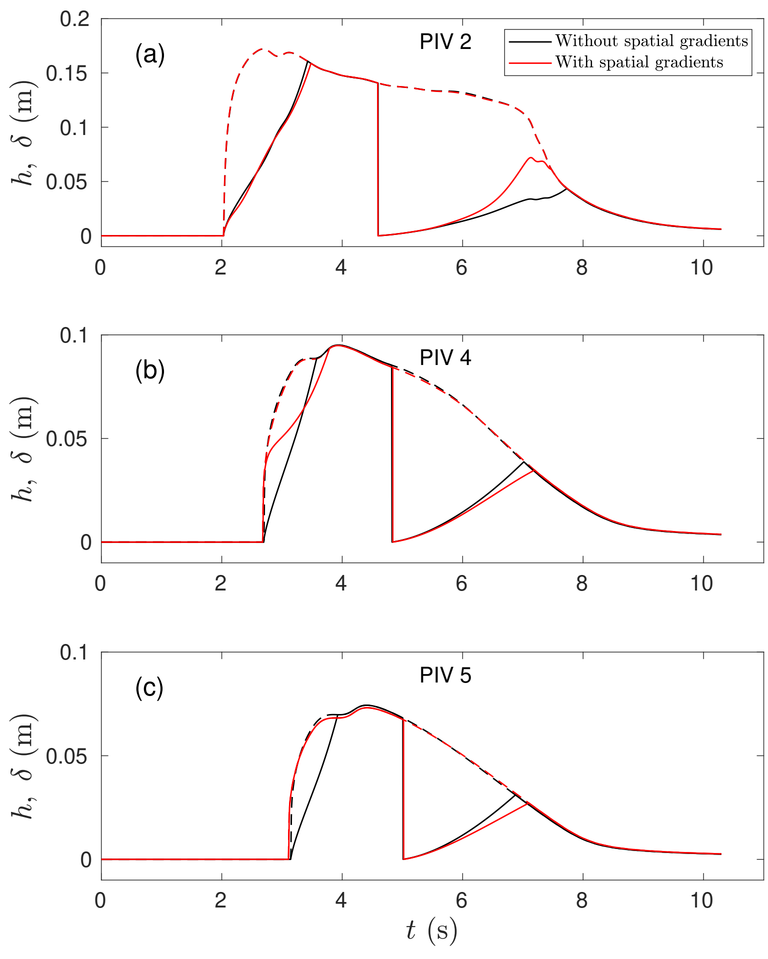

Figure 13: Boundary layer thickness δ (solid line) and water depth h (dashed line) at PIV 2, 4, and 5.

4.5. Velocity profile in the boundary layer

The velocity profiles are compared against the measured results in Fig. 14. Note that there are differences in water depths and velocities from the hydrodynamic models, which affect the comparison in velocity profiles.

At PIV 2, the boundary layer thickness in the uprush is overpredicted by both simulations with and without spatial gradients. In the backwash, the fast development of boundary layer at PIV 2 is well captured by the simulation with spatial gradients. At PIV 4 and 5, the more developed boundary layer in the early unprush and less developed boundary layer in the backwash are better captured by the simulation with spatial gradients.

The velocity profiles are generally well simulated at PIV 4 and 5 in the backwash. However, the modelled water depth is larger for similar U_0 values, which corresponds to larger depth-averaged velocity magnitudes, consistent with that observed in Fig. 11.

4.6. Bed shear stress

The bed shear stresses at PIV 2, 4 and 5 are shown in Fig. 15. The maximum bed shear stress occurs at the swash front, and the bed shear stress is larger in the backwash, which is consistent with the experimental findings of Howe et al. (2019).

The numerical simulations generally underestimate the bed shear stress at PIV 2, but slightly overpredict the bed shear stress at PIV 4 and 5. However, at all measuring stations the backwash velocity magnitudes are overestimated (see Fig. 11), which indicates the dependence of τ_b on effects other than u (U_0) alone. The overall better correspondence between simulated and measured τ_b at PIV4 and 5 is also reflected in the better reproduction in $U(z)$ (Fig. 14(b) and (c)).

The difference between simulations with and without spatial gradients is only noticeable in the early stage of inundation at PIV 4 and 5; the bed shear stress is smaller when spatial gradients are considered because of the more developed boundary layer. The peak in τ_b in the uprush also arrives slightly earlier, especially at PIV5. Again, this is linked to a fully developed boundary layer at the tip. At the tip, however, measurements of τ_b are mostly absent, and show much scatter, due to the difficulty in obtaining measurements there (Kikkert et al., 2012). However, there does seem to be some evidence that the inclusion of spatial gradients is indeed capturing τ_b a little better in the uprush.

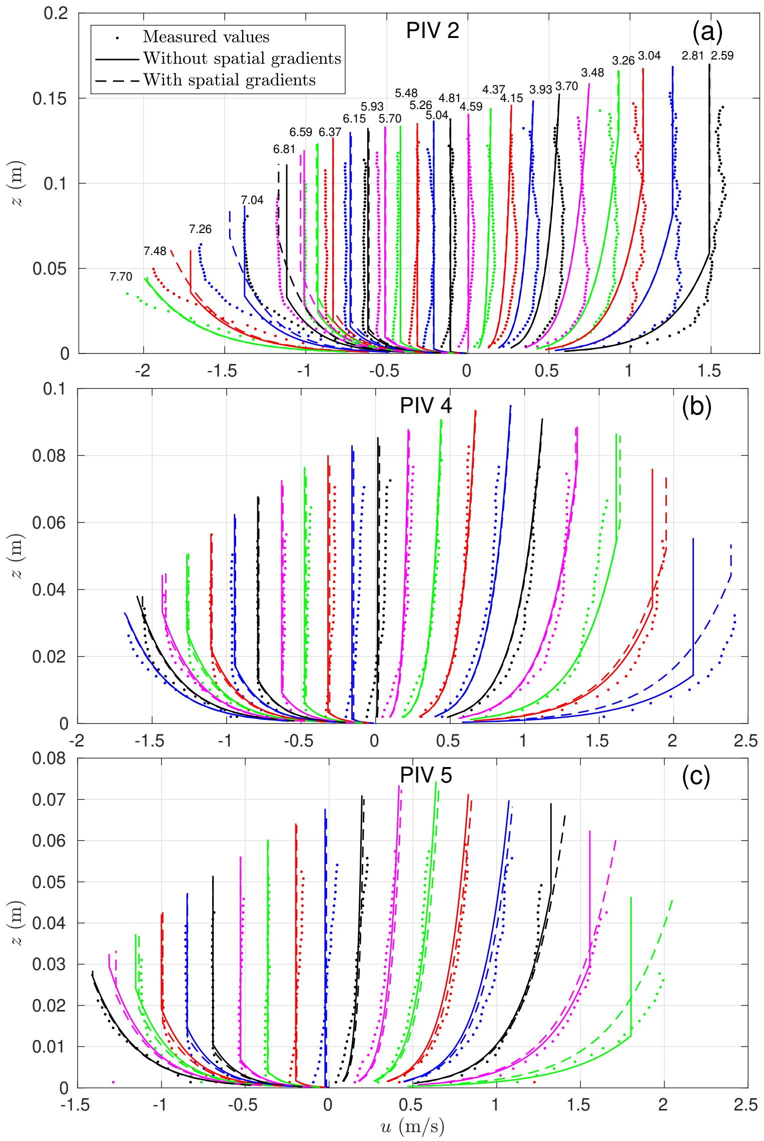

Figure 14: Comparison between the predicted (solid and dashed coloured lines) and measured (dots) profiles for the horizontal velocity for IMP015 set at PIV 2, 4 and 5. The values above the velocity profiles in (a) indicate times at which the velocity profiles are shown.

The bed shear stress is slightly larger at PIV 4 and 5 in the backwash because of the thinner boundary layer with spatial gradients. However, the difference of bed shear stress in the backwash is hard to discern.

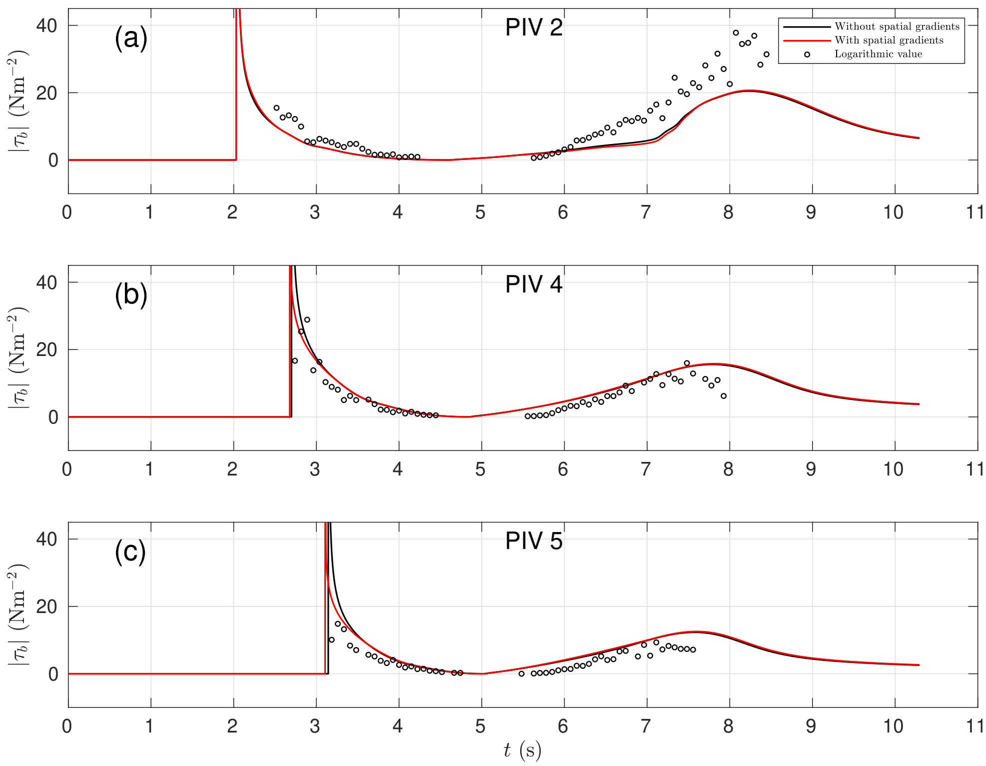

Figure 15: Comparison of bed shear stresses at PIV 2, 4 and 5. Circles: values estimated from measured velocity profiles; solid lines: numerical results.

Time series of $\tau_{b,wo}/\tau_{b,w}$ are shown in Fig. 16. Differences are generally smaller than for the Carrier and Greenspan (1958) case, except at the beginning of uprush and backwash, at which $\tau_{b,wo}$ is larger. These differences are in part caused by the aforementioned more well-developed boundary layer at the swash tip in the uprush when spatial gradients are included, as well as by small phasing differences. The large peak values occur because of the phasing differences. Note that shortly following these peak values, the ratio dips such that $\tau_{b,w} > \tau_{b,wo}$, particularly at the seaward extent of the swash (PIV 2), again indicating that the spatial gradients may contribute to onshore sediment movement at the beginning of the uprush. In the backwash at PIV2 we also see reduced bed shear stress in the presence of spatial gradients, also suggesting reduced offshore sediment transport in the backwash.

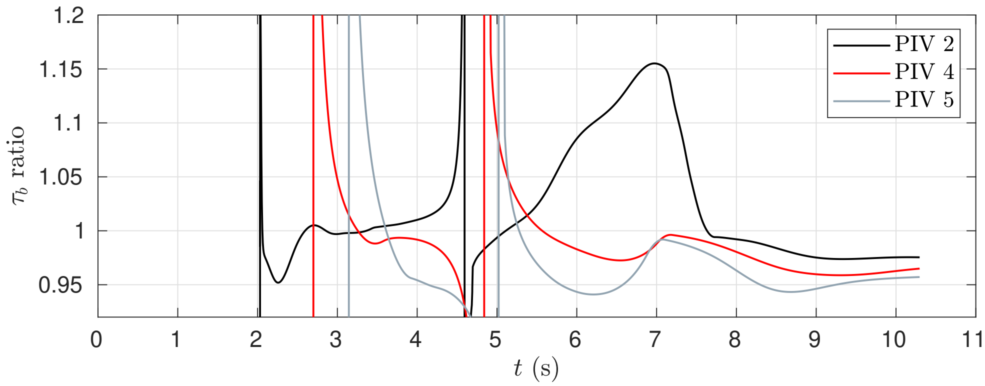

Figure 16: Time series of $\tau_{b,wo}/\tau_{b,w}$ at PIV 2, 4 and 5.

5. Conclusions

The boundary layer model used by Briganti et al. (2011) is extended to include spatial gradients in velocity and boundary layer thickness. This boundary layer model is incorporated in a NSWE hydrodynamic model solved by Specified Time Interval Method of Characteristics.

The periodic waves formulated by Carrier and Greenspan (1958) are simulated numerically with close agreement with the exact solutions, and the corresponding boundary layer development is examined. The results show that the boundary layer also develops periodically. The boundary layer grows in the uprush, vanishes at flow reversal, and grows again, more slowly in the backwash. The inclusion of spatial gradients makes a larger difference in the lower swash zone and further offshore, where it thins the boundary layer in the onshore flow and thickens it in the offshore flow. Therefore, the bed shear stress is enhanced in the uprush, and slightly diminished in the backwash. This implies that spatial gradients might enhance onshore sediment transport in non-breaking waves, potentially contributing to the formation of a swash berm, and thereby helping formation of cusps, by providing another onshore sediment transport mechanism in addition to infiltration (Dodd et al., 2008).

The Kikkert et al. (2012) dam-break swash event is also simulated and the numerical results are compared against laboratory measurements. The shoreline trajectories are in very good agreement with the measurements.

The velocities at PIV 2, 4, 5 in the later backwash agree more closely with the measurements than those of Briganti et al. (2011). Overall the Briganti et al. (2011) model resulted in lower values of τ_b in the backwash, as the comparison between Fig. 15 of the present work and Fig. 13 of Briganti et al. (2011) shows. However, the numerical simulations still overestimate the backwash velocities. The differences in the backwash velocities predicted by Briganti et al. (2011) and this work are most likely due to the differences in the NSWE solver and particularly the shoreline treatment. The shoreline motion shown in Fig. 9 implies the faster movement of the shoreline in the backwash predicted by Briganti et al. (2011).

For this bore-driven swash event the inclusion of spatial gradients results in an earlier initial increase of boundary layer thickness in the uprush, particularly higher up the swash. This also implies a diminution in slightly later uprush bed shear stress predictions, compared to those from the spatially uniform momentum integral model of Briganti et al. (2011). These results are consistent with the modelling of advection of the boundary layer near to the tip in the present model, which also shows consistency with earlier work (Baldock, 2018; Baldock and Torres-Freyermuth, 2020), and with the experiments of Kikkert et al. (2012). The results also show that the inclusion of spatial gradients makes little difference to the hydrodynamics as described in terms of depth and depth-averaged velocity. The boundary layer as predicted by the present method shows largest significant differences from that predicted by the equivalent spatially uniform method primarily at and near the base of the swash, in the flow near bore collapse, and in the region just seaward of the backwash bore.

In summary, the nonuniformities of velocity and boundary layer have a clear effect in wave-driven swash, potentially promoting onshore sediment transport; the feedback onto the flow still needs to be examined. In bore-driven swash significant differences are also observed in the boundary layer predictions. Differences in τ_b are smaller, but, near the base of the swash, spatial gradients are also expected to promote onshore sediment movement, both in the uprush and backwash. The most notable qualitative differences in bed shear stress are observed in the upper swash, connected to advection of the boundary layer at the tip. This extended momentum integral approach, including spatial gradients in the boundary layer, captures some realistic effects, compared to its spatially uniform counterpart, whilst remaining computationally achievable in the context of NSWE modelling. A remaining limitation is that of the logarithmic boundary layer.

Acknowledgement

This work is supported by Natural Science Foundation of China (project code 51811530012) and The Swedish Foundation for International Cooperation In Research and Higher Education (project code CH2017-7218). Their support is gratefully acknowledged. We are grateful to the comments and suggestions of two anonymous reviewers.

Appendix A. Free stream velocity

The logarithmic velocity profile inside the boundary layer is

$$U(x,z,t) = \frac{U_f}{\kappa}\ln\left(\frac{z}{z_0}\right). \tag{A.1}$$

If $\delta \leq h$, the free stream velocity is

$$U_0 = \frac{U_f}{\kappa}\ln\left(\frac{z_0+\delta}{z_0}\right) = \frac{U_f}{\kappa}Z. \tag{A.2}$$

The depth-averaged velocity can be related to the horizontal velocities in the vertical profile,

$$\begin{aligned} u &= \frac{1}{h}\left[\int_{z_0}^{\delta+z_0}\frac{U_f}{\kappa}\ln\left(\frac{z}{z_0}\right)dz + (h-\delta)U_0\right] \\ &= \frac{1}{h}\left[\frac{U_f}{\kappa}\left((\delta+z_0)Z-\delta\right) + (h-\delta)U_0\right] \\ &= \frac{1}{h}\left[U_0\left((\delta+z_0)-\frac{\delta}{Z}\right) + (h-\delta)U_0\right], \end{aligned} \tag{A.3}$$

which thus gives

$$U_0 = \frac{hu}{z_0+h-\delta/Z}. \tag{A.4}$$

In the case $\delta > h$, the assumptions of $\delta = h$ and $U(z = z_0+h) = U_0$ are introduced. Thus,

$$U_0 = \frac{U_f}{\kappa}\ln\left(\frac{z_0+h}{z_0}\right). \tag{A.5}$$

The depth-averaged velocity is therefore

$$\begin{aligned}
u &= \frac{1}{h}\left[\int_{z_0}^{z_0+h} \frac{U_f}{\kappa}\ln\left(\frac{z}{z_0}\right)dz\right] \\
&= \frac{1}{h}\frac{U_f}{\kappa}\left((h+z_0)\ln\left(\frac{z_0+h}{z_0}\right)-h\right) && \text{(A.6)}\\
&= \frac{1}{h}\frac{U_0}{\ln\left(\frac{z_0+h}{z_0}\right)}\left((h+z_0)\ln\left(\frac{z_0+h}{z_0}\right)-h\right) && \text{(A.7)}\\
\Rightarrow U_0 &= \frac{hu\ln\left(\frac{z_0+h}{z_0}\right)}{(h+z_0)\ln\left(\frac{z_0+h}{z_0}\right)-h}. && \text{(A.8)}
\end{aligned}$$

Appendix B. Bed shear stress at the swash tip

The boundary layer and in particular bed shear stress at the moving swash tip need careful treatment. Consider the fundamental assumption of the boundary layer form

$$U(z) = \frac{U_f}{\kappa}\ln\left(\frac{z}{z_0}\right) \Rightarrow U_0 = \frac{U_f}{\kappa}\ln\left(\frac{z_0+\delta}{z_0}\right) = \frac{U_f}{\kappa}Z. \tag{B.1}$$

Now, if $\delta \to 0$ at the tip, then, because $U_0 \neq 0$ at the tip, this $\Rightarrow U_f \to \infty$. Instead, we do not insist that $\delta \to 0$ anywhere, but impose a minimum value for h.

Accordingly, we take $h \to nz_0$ at the tip, then, utilising (A.6) we get:

$$\tau_b = \rho\kappa^2\frac{n^2}{\{(n+1)\ln(1+n)-n\}^2}u^2 = \rho\kappa^2 f_n u^2 \tag{B.2}$$

Note that (B.2) decreases as n increases, but that the sequence $\{f_n\}$ decreases increasingly slowly as $n \to \infty$. Note also that $\kappa^2 f_n \equiv c_d$, where c_d is a Chezy friction coefficient.

We can then evaluate the effect of varying n on the $\tau_b(x_s)$ values. For both Carrier and Greenspan (1958) case and Kikkert et al. (2012) case, we have $z_0 = 0.1$ mm. If we take $u = 0.1$ m/s, the variations of $\kappa^2 f_n$ and τ_b with h are shown in Table B.3 alongside typical values for a friction coefficient $c_d = 0.025$.

Table B.3: Variations of $\kappa^2 f_n$ and τ_b (N/m^2) with $h = nz_0$ (m).

n	h	$\kappa^2 f_n$	c_d	$\tau_b(x_s)$	$\tau_b(c_d)$
1	0.0001	1.0722	0.0250	10.722	0.250
2	0.0002	0.3811	0.0250	3.811	0.250
3	0.0003	0.2223	0.0250	2.223	0.250
5	0.0005	0.1210	0.0250	1.210	0.250
10	0.0010	0.0597	0.0250	0.597	0.250
50	0.0050	0.0177	0.0250	0.177	0.250
100	0.0100	0.0119	0.0250	0.119	0.250

Note the very large decrease in $\tau_b(x_s)$ from $h = z_0$ to $h = 2z_0$. Thereafter, the decrease gets progressively smaller.

In the numerical simulations, we adopt $h = 10z_0$ at the tip in the BBL submodel. $h = 10z_0$ is also used for the calculation of bed shear stress at the grid next to the tip if $h < 10z_0$ there.

Appendix C. Early time analytical approximations

It is assumed that Eq. (11) describes the boundary layer development, starting from (uprush in the swash zone) the time of inundation ($U_0(t = t_0) \neq 0$), or the time of flow reversal ($U_0(t = t_0) = 0$), for all x. In both cases the initial condition is $Z(t_0) = 0$, where $t = t_0$ represents either the time of inundation or time of flow reversal.

As $t \to t_0$, Eqs. (10) and (11) become

$$\frac{\partial Z}{\partial t} \sim \frac{\kappa^2}{z_0}\frac{2}{Z^2}|U_0(t)| - Z\frac{\partial}{\partial t}\ln U_0(t). \tag{C.1}$$

If we now treat partial derivatives as ordinary derivatives, then Eq. (C.1) becomes a Bernoulli equation. Under the transformation $w(t) = Z(t)^3$ we then get

$$\frac{dw}{dt} + 3\frac{d}{dt}\ln U_0(t)w \sim 6\frac{\kappa^2}{z_0}|U_0(t)|. \tag{C.2}$$

Transforming back we get a general solution

$$Z^3 \sim 6\frac{\kappa^2}{z_0}\frac{1}{U_0^3}\int^t |U_0(t')|U_0^3(t')\,dt' + \frac{C}{U_0^3}, \tag{C.3}$$

where C is a constant of integration. If we then expand U_0 in a Taylor series about $t = t_0$ we get two short-time asymptotic solutions. In the swash uprush ($U_0(t_0) > 0$, $\frac{dU_0}{dt}$ bounded):

$$Z \sim \left\{ 6\frac{\kappa^2}{z_0}\frac{U}{|U|}U_0(t_0)(t-t_0) \right\}^{\frac{1}{3}}, \tag{C.4}$$

and otherwise ($U_0(t_0) = 0$, $\frac{dU_0}{dt} \neq 0$):

$$Z \sim \left\{ \frac{6}{5}\frac{\kappa^2}{z_0}\frac{U}{|U|} \left.\frac{dU_0}{dt}\right|_{t=t_0} (t-t_0)^2 \right\}^{\frac{1}{3}}. \tag{C.5}$$

Note that as $Z \to 0$, in Eq. (C.1) the boundary layer growth term overwhelms the thinning effect of the acceleration, which is why the acceleration in Eq. (C.5) promotes boundary layer growth. Thus, both solutions have unbounded growth in Z from $Z(t_0)$.

Appendix D. Derivation of the shock condition for boundary layer thickness δ

$$\text{Eq. (3) - Eq. (4)} \Rightarrow \frac{\partial(U_0-U)}{\partial t} + \frac{1}{2}\frac{\partial(U_0^2-U^2)}{\partial x} = -\frac{1}{\rho}\frac{\partial\tau}{\partial z}. \tag{D.1}$$

Integrating it over the boundary layer,

$$\int_{z_0}^{z_0+\delta} \frac{\partial}{\partial t}(U_0-U)\,dz + \frac{1}{2}\int_{z_0}^{z_0+\delta}\frac{\partial}{\partial x}\left(U_0^2-U^2\right)dz = \frac{\tau_b}{\rho} = U_f^2$$

$$U_f^2 = \frac{\partial}{\partial t}\int_{z_0}^{z_0+\delta}(U_0-U)\,dz + \frac{1}{2}\frac{\partial}{\partial x}\int_{z_0}^{z_0+\delta}\left(U_0^2-U^2\right)dz. \tag{D.2}$$

Substituting Eq. (5) into (D.2) gives

$$\begin{aligned} U_f^2 &= \frac{\partial}{\partial t}\left(-z_0U_0 + \frac{U_f}{\kappa}\delta\right) + \frac{1}{2}\frac{\partial}{\partial x}\left(-z_0U_0^2 + 2\frac{U_f}{\kappa}U_0(z_0+\delta) + 2\frac{U_f^2}{\kappa^2}\delta\right) \\ &= \frac{\partial}{\partial t}\left(-z_0U_0 + \frac{U_0}{Z}\delta\right) + \frac{1}{2}\frac{\partial}{\partial x}\left(-z_0U_0^2 + 2\frac{U_0^2}{Z}(z_0+\delta) + 2\frac{U_0^2}{Z^2}\delta\right). \end{aligned} \tag{D.3}$$

Therefore, the shock condition for δ is

$$-W\left[-z_0U_0+\frac{U_0}{Z}\delta\right]_L^R+\frac{1}{2}\left[-z_0U_0^2+2\frac{U_0^2}{Z}(z_0+\delta)+2\frac{U_0^2}{Z^2}\delta\right]_L^R=0, \quad (D.4)$$

where the subscripts L and R represent the left and right sides of the bore.

If spatial gradients are neglected, Eq. (D.4) reduces to

$$\left[-z_0U_0+\frac{U_0}{Z}\delta\right]_L^R=0. \quad (D.5)$$

Appendix E. Carrier and Greenspan (1958) verification

The shoreline movement comparison between the numerical results and the analytical results (Carrier and Greenspan, 1958) are shown in Fig. E.17 with very close agreement. The maximum run up is slightly underpredicted (Fig. E.17).

References

G. F. Carrier, H. P. Greenspan, Water waves of finite amplitude on a sloping beach, J. Fluid Mech. 4 (1958) 97–109.

G. Kikkert, T. O'Donoghue, D. Pokrajac, N. Dodd, Experimental study of bore-driven swash hydrodynamics on impermeable rough slopes, Coastal Eng. 60 (2012) 149–166.

R. Briganti, N. Dodd, D. Pokrajac, T. O'Donoghue, Non linear shallow water modelling of bore-driven swash: Description of the bottom boundary layer, Coastal Eng. 58 (2011) 463–477.

N. Kobayashi, A. Wurjanto, Wave overtopping on coastal structures, ASCE J. Water. Port Coast. Ocean Eng. 115(2) (1989) 235–251.

N. Dodd, Numerical model of wave run-up, overtopping and regeneration, ASCE J. Water. Port Coast. Ocean Eng. 124(2) (1998) 73–81.

G. Bellotti, M. Brocchini, Swash zone boundary conditions for long-wave models, Coastal Eng. 52 (2005) 971–976.

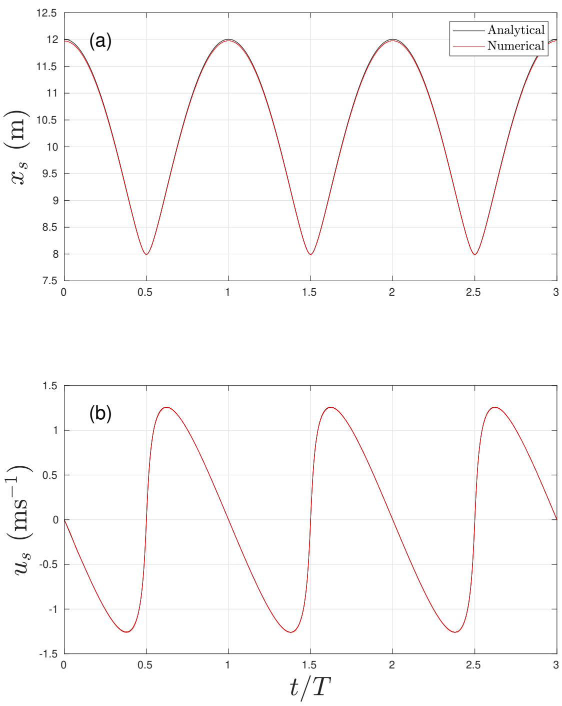

Figure E.17: The comparison of shoreline movement between numerical and analytical results with $A = 0.8$.

J. A. Puleo, K. T. Holland, N. G. Plant, D. N. Slinn, D. M. Hanes, Fluid acceleration effects on suspended sediment transport in the swash zone, J. Geophys. Res. 108 (2003).

J. A. Puleo, F. Farhadzadeh, N. Kobayashi, Numerical simulation of swash zone fluid accelerations, J. Geophys. Res. 112 (2007).

A. Torres-Freyermuth, J. A. Puleo, D. Pokrajac, Modeling swash-zone hydrodynamics and shear stresses on planar slopes using Reynolds-Averaged Navier-Stokes equations, J. Geophys. Res. 118 (2013) 1019–1033.

R. Briganti, A. Torres-Freyermuth, T. E. Baldock, M. Brocchini, N. Dodd, T.-J. Hsu, Z. Jiang, Y. Kim, J. C. Pintado-Patiño, M. Postacchini, Advances in numerical modelling of swash zone dynamics, Coastal Eng. 115 (2016) 26–41.

T. E. Baldock, A. Torres-Freyermuth, Numerical study of the flow structure at a swash tip propagating over a rough bed, Coastal Eng. 161 (2020) 103729.

M. P. Barnes, T. E. Baldock, A Lagrangian model for boundary layer growth and bed shear stress in the swash zone, Coastal Eng. 57 (2010) 385–396.

J. Fredsøe, R. Deigaard, Mechanics of Coastal Sediment Transport, volume 3 of *Advanced Series on Ocean Engineering*, World Scientific, Singapore, 1993.

T. O'Donoghue, D. Pokrajac, L. J. Hondebrink, Laboratory and numerical study of dambreak-generated swash on impermeable slopes, Coastal Eng. 57 (2010) 513–530.

M. P. Barnes, T. O'Donoghue, J. M. Alsina, T. E. Baldock, Direct bed shear stress measurements in bore-driven swash, Coastal Eng. 56 (2009) 853–867.

A. Ruju, D. Conley, G. Masselink, M. Austin, J. Puleo, T. Lanckriet, D. Foster, Boundary layer dynamics in the swash zone under large-scale laboratory conditions, Coastal Eng. 113 (2016) 47–61.

D. J. Needham, R. D. Hey, On nonlinear simple waves in alluvial river flows: a theory for sediment bores, Phil. Trans. Roy. Soc. Lond. A 334 (1991) 25–53.

F. Zhu, N. Dodd, The morphodynamics of a swash event on an erodible beach, J. Fluid Mech. 762 (2015) 110–140.

S. Mungkasi, S. G. Roberts, Approximations of the Carrier-Greenspan periodic solution to the shallow water wave equations for flows on a sloping beach, Int. J. Numercal Meth. Fluids 69 (2012) 763–780.

G. Kikkert, D. Pokrajac, T. O'Donoghue, Bed shear stress in bore-generated swash on steep beaches, in: Proc. Coastal Dynamics '09, A.S.C.E., Tokyo, Japan, pp. U56–U57.

F. Engelund, E. Hansen, A monograph on sediment transport, Technical Report, Teknisk Forlag, Copenhagen, Denmark., 1967.

T. E. Baldock, "Bed shear stress, surface shape and velocity field near the tips of dam-breaks, tsunami and wave runup" by Peter Nielsen, Coastal Eng. 142 (2018) 77–81.

D. Howe, C. E. Blenkinsopp, I. L. Turner, T. E. Baldock, J. A. Puleo, Direct measurements of bed shear stress under swash flows on steep laboratory slopes at medium to prototype scales, Journal of Marine Science and Engineering 7 (2019) 358.

N. Dodd, A. Stoker, D. Calvete, A. Sriariyawat, On beach cusp formation, J. Fluid Mech. 597 (2008) 145–169.